2014-04-01

Combined Effect of Rotation and Topography on Shoaling Oceanic Internal Solitary Waves

Grimshaw, R

10.1175/jpo-d-13-0194.1
Journal of Physical Oceanography
American Meteorological Society

Combined Effect of Rotation and Topography on Shoaling Oceanic Internal Solitary Waves

ROGER GRIMSHAW

Department of Mathematical Sciences, Loughborough University, Loughborough, United Kingdom

CHUNCHENG GUO

Geophysical Institute, University of Bergen, Bergen, Norway

KARL HELFRICH

Department of Physical Oceanography, Woods Hole Oceanographic Institution, Woods Hole, Massachusetts

VASILIY VLASENKO

School of Marine Science and Engineering, Plymouth University, Plymouth, United Kingdom

(Manuscript received 10 September 2013, in final form 7 December 2013)

ABSTRACT

Internal solitary waves commonly observed in the coastal ocean are often modeled by a nonlinear evolution equation of the Korteweg–de Vries type. Because these waves often propagate for long distances over several inertial periods, the effect of Earth's background rotation is potentially significant. The relevant extension of the Kortweg–de Vries is then the Ostrovsky equation, which for internal waves does not support a steady solitary wave solution. Recent studies using a combination of asymptotic theory, numerical simulations, and laboratory experiments have shown that the long time effect of rotation is the destruction of the initial internal solitary wave by the radiation of small-amplitude inertia–gravity waves, and the eventual emergence of a coherent, steadily propagating, nonlinear wave packet. However, in the ocean, internal solitary waves are often propagating over variable topography, and this alone can cause quite dramatic deformation and transformation of an internal solitary wave. Hence, the combined effects of background rotation and variable topography are examined. Then the Ostrovsky equation is replaced by a variable coefficient Ostrovsky equation whose coefficients depend explicitly on the spatial coordinate. Some numerical simulations of this equation, together with analogous simulations using the Massachusetts Institute of Technology General Circulation Model (MITgcm), for a certain cross section of the South China Sea are presented. These demonstrate that the combined effect of shoaling and rotation is to induce a secondary trailing wave packet, induced by enhanced radiation from the leading wave.

1. Introduction

Internal solitary waves (ISW) commonly observed in the coastal ocean are often modeled by the Korteweg–de Vries (KdV) equation [see the reviews by Grimshaw (2001) and Helfrich and Melville (2006), for instance]. In a reference frame moving with a linear long-wave speed c, the KdV equation is

$$\eta_t + \mu\eta\eta_x + \lambda\eta_{xxx} = 0. \tag{1}$$

Here, $\eta(x, t)$ is the amplitude of the linear long-wave mode $\phi(z)$ corresponding to a linear long wave with phase speed c, which is determined from the modal equation

$$[\rho_0(c-u_0)^2\phi_z]_z - g\rho_{0z}\phi = 0 \quad \text{for} \quad -h < z < 0, \quad \text{and} \tag{2}$$

$$\phi = 0 \quad \text{at} \quad z = -h \quad \text{and} \quad (c-u_0)^2\phi_z = g\phi \quad \text{at} \quad z = 0. \tag{3}$$

Corresponding author address: Karl Helfrich, WHOI, MS 21, Woods Hole, MA 02543.
E-mail: khelfrich@whoi.edu

DOI: 10.1175/JPO-D-13-0194.1

Here, t is time, x is the horizontal coordinate, $\rho_0(z)$ is the stably stratified background density stratification, and $u_0(z)$ is a horizontal background shear current. The coefficients μ and λ are given by

$$I\mu = 3\int_{-h}^{0} \rho_0 (c-u_0)^2 \phi_z^3 \, dz, \tag{4}$$

$$I\lambda = \int_{-h}^{0} \rho_0 (c-u_0)^2 \phi^2 \, dz, \quad \text{and} \tag{5}$$

$$I = 2\int_{-h}^{0} \rho_0 (c-u_0) \phi_z^2 \, dz. \tag{6}$$

Oceanic internal waves are often observed to propagate for long distances over several inertial periods, and hence the effect of the earth's background rotation is potentially significant. The large ISWs in the South China Sea are prominent examples (Zhao and Alford 2006; Alford et al. 2010). There are also numerous remote sensing images throughout the coastal oceans that show multiple wave packets (Jackson 2004), separated by the M_2 period, indicating that the ISWs persist over periods longer than the local inertial period. The relevant extension of the KdV equation (1) that includes the effects of rotation is the Ostrovsky equation, derived initially by Ostrovsky (1978) and later for waves in channels by Grimshaw (1985):

$$(\eta_t + \mu\eta\eta_x + \lambda\eta_{xxx})_x = \gamma\eta. \tag{7}$$

The background rotation is represented by the coefficient γ, given by

$$I\gamma = f^2 \int_{-h}^{0} \rho_0 \Phi \phi_z \, dz \quad \text{and}$$
$$\rho_0 (c-u_0)\Phi = \rho_0 (c-u_0)\phi_z - (\rho_0 u_0)_z \phi, \tag{8}$$

where f is the Coriolis parameter. In the absence of a background current, then $\gamma = f^2/2c$. The more general expression (8) was derived recently by Alias et al. (2013) and Grimshaw (2013). For oceanic internal waves in the absence of a background current, $\lambda\gamma > 0$ [see (5) and (8)], and then it is known that (7) does not support steady solitary wave solutions [see Grimshaw and Helfrich (2012) and the references therein]. The simplest explanation is that then the additional term on the right-hand side of (7) removes the spectral gap in which solitary waves exist for the KdV equation, and hence no solitary waves are expected to occur. Note that when there is a nonzero background current, then it is possible, but very unlikely in oceanic conditions, that $\lambda\gamma < 0$ (Grimshaw 2013). Nevertheless, if this should occur, then the Ostrovsky equation (7) does support a solitary wave, albeit of envelope type [see Grimshaw et al. (1998b) and Obregon and Stepanyants (1998)]. Further, Grimshaw and Helfrich (2008, 2012) and Grimshaw et al. (2013) have shown that the long time effect of rotation is the destruction of the initial ISW by the radiation of small-amplitude inertia–gravity waves and the eventual emergence of a coherent, steadily propagating, nonlinear wave packet.

However, in the ocean ISWs often propagate over variable topography, and this alone can cause quite dramatic deformation and transformation of an ISW. These effects include formation of a long trailing tail, that is, a nearly uniform isopycnal displacement, behind a wave propagating into shallower depths, the topographic scattering, or fissioning, of the wave into two or more solitary waves, and other more subtle situations, including the reversal of wave polarity and formation of breathers, which depend sensitively on the variations in magnitude and sign of the coefficients of the quadratic and cubic nonlinear terms [the latter is not included here in (7) for simplicity]. See the recent review by Grimshaw et al. (2010) for a more complete discussion. Thus, individually the effects of rotation and topography can have significant effects on ISW evolution in realistic oceanic situations. Their joint effects are much less clear. Hence, in this paper we examine the combined effects of background rotation and variable topography.

In section 2, we present the variable coefficient Ostrovsky equation and the analysis of the combined effects of topography and rotation on wave evolution. Then, in section 3, we describe some numerical simulations for a transect of the South China Sea (SCS), selected as it is a recognized "hot spot" for internal waves. The simulations use both the variable coefficient Ostrovsky equation and a fully nonlinear ocean model, the Massachusetts Institute of Technology General Circulation Model (MITgcm). We conclude in section 4.

2. Variable coefficient Ostrovsky equation

a. Formulation

In the presence of a slowly varying background, the KdV (1) is replaced by the variable coefficient KdV equation, first derived by Johnson (1973) for water waves and then by Grimshaw (1981) for internal waves [for a recent review, see Grimshaw et al. (2010)]. In an analogous manner, when the bottom topography and hydrography vary slowly in the x direction, the Ostrovsky equation (7) is replaced by the variable coefficient Ostrovsky equation:

$$\left(\eta_t + c\eta_x + \frac{cQ_x}{2Q}\eta + \mu\eta\eta_x + \lambda\eta_{xxx}\right)_x = \gamma\eta. \tag{9}$$

Here, as above, $\eta(x, t)$ is the amplitude of the wave. The coefficients, c, μ, λ, and γ are defined as above in section 1, while Q is the linear magnification factor, given by

$$Q = Ic^2. \tag{10}$$

It is defined so that $Q\eta^2$ is the wave action flux. Each of these coefficients is a slowly varying function of x. The formal derivation assumes the usual KdV and Ostrovsky equation balance and in addition assumes that the waveguide properties (i.e., the coefficients c, Q, μ, and λ) vary slowly so that Q_x/Q for instance is of the same order as the dispersive, nonlinear, and rotation terms (see Grimshaw 2013).

The first two terms in (9) are the dominant terms, and it is then useful to make the transformation

$$A = \sqrt{Q}\eta, \quad T = \int^x \frac{dx}{c}, \quad \text{and} \quad X = T - t. \tag{11}$$

Substitution into (9) yields, to the same order of approximation as in the derivation of (9),

$$(A_T + \alpha A A_X + \delta A_{XXX})_X = \beta A, \tag{12}$$

$$\alpha = \frac{\mu}{c\sqrt{Q}}, \quad \delta = \frac{\lambda}{c^3}, \quad \text{and} \quad \beta = \gamma c. \tag{13}$$

Here, the coefficients α, δ, and β are functions of T alone. Note that although T is a variable along the spatial path of the wave, we shall subsequently refer to it as the "time." Similarly, although X is a temporal variable, in a reference frame moving with speed c, we shall subsequently refer to it as a "space" variable.

Alternatively, (12) can be written as

$$A_T + \alpha A A_X + \delta A_{XXX} = \beta B \quad \text{and} \quad B_X = A. \tag{14}$$

There are two conservation laws for localized solutions of (14):

$$\int_{-\infty}^{\infty} A\, dX = 0 \quad \text{and} \tag{15}$$

$$\frac{\partial}{\partial T}\int_{-\infty}^{\infty} A^2\, dX = 0. \tag{16}$$

The first, (15), is a zero mass condition, and note that when A is localized, then so is B; indeed B, like A, also has zero mean. The second, (16), expresses wave action flux conservation.

b. Extinction of solitary waves

1) SLOWLY VARYING SOLITARY WAVE

As mentioned already, the Ostrovsky equation with constant coefficients does not support solitary waves, assuming here that we have the usual case when $\lambda\gamma > 0$. If one imposes an initial condition of a KdV solitary wave, then this decays by the radiation of inertia–gravity waves and is extinguished in finite time [see (29) below], being eventually replaced by a nonlinear envelope wave packet (see Grimshaw and Helfrich 2008, 2012; Grimshaw et al. 2013). Here, we examine this same scenario when there is a background of variable topography and hydrology. In this section, we revisit the decay of an initial KdV solitary wave, using the same asymptotic procedure described by Grimshaw et al. (1998a) for the case when the coefficients are constants. Thus, we now suppose that the coefficients α and δ are slowly varying, and that β is small, and write

$$\alpha = \alpha(\tau), \quad \delta = \delta(\tau), \quad \beta = \epsilon\tilde{\beta}, \quad \tau = \epsilon T, \quad \text{and} \quad \epsilon \ll 1. \tag{17}$$

We seek a standard multiscale expansion for a modulated wave, namely,

$$A = A^{(0)}(\theta, \tau) + \epsilon A^{(1)}(\theta, \tau) + \cdots, \quad \text{where} \tag{18}$$

$$\theta = X - \frac{1}{\epsilon}\int^{\tau} V(\tau)\, d\tau. \tag{19}$$

Substitution into (12) yields at the leading orders

$$-VA^{(0)}_\theta + \alpha A^{(0)} A^{(0)}_\theta + \delta A^{(0)}_{\theta\theta\theta} = 0, \tag{20}$$

$$-VA^{(1)}_\theta + \alpha[A^{(0)}A^{(1)}]_\theta + \delta A^{(0)}_{\theta\theta\theta} = -A^{(0)}_\tau + \tilde{\beta}B^{(0)}, \qquad B^{(0)}_\theta = A^{(0)}. \tag{21}$$

Each of these is essentially an ordinary differential equation with θ as the independent variable and τ as a parameter.

The solution for $A^{(0)}$ is taken to be the solitary wave:

$$A^{(0)} = a\,\mathrm{sech}^2(K\theta), \tag{22}$$

$$\text{where} \quad V = \frac{\alpha a}{3} = 4\delta K^2. \tag{23}$$

At the next order, we seek a solution of (21) for $A^{(1)}$, which is bounded as $\theta \to \pm\infty$, and in fact $A^{(1)} \to 0$ as $\theta \to \infty$. The adjoint equation to the homogeneous part of (21) is

$$-VA_\theta^{(1)} + \alpha A^{(0)} A_\theta^{(1)} + \delta A_{\theta\theta\theta}^{(1)} = 0. \tag{24}$$

Two solutions are 1, $A^{(0)}$; while both are bounded, only the second solution satisfies the condition that $A^{(1)} \to 0$ as $\theta \to \infty$. A third solution can be constructed using the variation-of-parameters method, but it is unbounded as $\theta \to \pm\infty$. Hence, only one orthogonality condition can be imposed, namely, that the right-hand side of (21) is orthogonal to $A^{(0)}$, which leads to

$$\frac{\partial}{\partial \tau} \int_{-\infty}^{\infty} [A^{(0)}]^2 \, d\theta = \tilde{\beta} [B^{(0)}(\theta \to -\infty)]^2. \tag{25}$$

Note that here $B^{(0)}(\theta \to \infty) = 0$, and so

$$B^{(0)} = \int_{\infty}^{\theta} A^{(0)} \, d\theta = -\frac{a}{K}[1 - \tanh(K\theta)]. \tag{26}$$

As the solitary wave (22) has just one free parameter (e.g., the amplitude a), this equation suffices to determine its variation. Substituting (22) and (23) into (25) leads to the law

$$\mathcal{A}^{1/2} \frac{\partial \mathcal{A}}{\partial \tau} = -3\tilde{\beta} \left(\frac{12\delta}{\alpha} \right)^{2/3} \mathcal{A} \quad \text{and} \quad \mathcal{A} = \left(\frac{12\delta}{\alpha} \right)^{1/3} a. \tag{27}$$

This has the solution

$$\mathcal{A}^{1/2} = \mathcal{A}_0^{1/2} - \tilde{\beta} s \quad \text{and} \quad s = \int_0^{\tau} \left(\frac{12\delta}{\alpha} \right)^{2/3} d\tau, \tag{28}$$

where $\mathcal{A}_0 = \mathcal{A}(\tau = 0)$. Thus, as for the constant depth case, the solitary wave is extinguished in finite time. For constant depth, the extinction time is, in dimensional coordinates,

$$t_e = \frac{1}{\beta} \left(\frac{\alpha a_0}{12\delta} \right)^{1/2} = \frac{1}{\gamma} \left(\frac{\mu \eta_0}{12\lambda} \right)^{1/2}, \tag{29}$$

where here we recall that time is really ''distance'' along the path [see (11)]. Note that we have assumed that $\delta > 0$, $\beta > 0$, which is the case for waves propagating in the positive x direction, and have also assumed for simplicity that $\alpha > 0$ and so $a > 0$. But if $\alpha < 0$, then $a < 0$ and we can simply replace δ, a with $|\delta|$, $|a|$ in these expressions.

We now recall that (12) has two conservation laws (15) and (16). The condition (25) is easily recognized as the leading order expression for conservation of local wave action flux. But because this completely defines the slowly varying solitary wave, we now see that this cannot simultaneously conserve total mass [see (15)]. This is apparent when one examines the solution of (21) for $A^{(1)}$, from which it is readily shown that although $A^{(1)} \to 0$ as $\theta \to \infty$, $A^{(1)} \to \beta B^{(0)}(\theta \to -\infty)\theta/V$ as $\theta \to -\infty$. This nonuniformity in the slowly varying solitary wave has been recognized for some time [see, for instance, Grimshaw and Mitsudera (1993) and the references therein]. The remedy is the construction of a trailing tail A_s of small amplitude $O(\epsilon)$ but long length scale $O(1/\epsilon)$, which thus has $O(1)$ mass, but $O(\epsilon)$ wave action flux. It resides behind the solitary wave and to leading order becomes trailing inertia–gravity waves.

In more detail we find that

$$\epsilon A^{(1)} \sim -\frac{2\beta a \theta}{KV}, \quad \text{as} \quad \theta \to -\infty. \tag{30}$$

To the leading order, the trailing wave is a linear long wave. At the location of the solitary wave, it is given by

$$A \sim b \sin(k\theta), \quad \text{where} \quad Vk^2 = \beta. \tag{31}$$

Here, we assume that this trailing wave and the solitary wave must have the same phase θ in order to match. Hence, k is found from the linear long-wave dispersion relation and hence is determined from V. Setting $k\theta \ll 1$ in (31) and matching with (30) yields

$$bk = -\frac{2\beta a}{KV}, \quad \text{so that} \quad b = -\frac{6\beta}{Kk\alpha} = -\frac{12(\beta\delta)^{1/2}}{\alpha}$$
$$\text{and} \quad \eta_s = -\frac{12(\gamma\lambda Q)^{1/2}}{\mu}. \tag{32}$$

This determines the trailing wave amplitude b or η_s in terms of the original variables. Note that it is proportional to $\beta^{1/2}$ and interestingly is independent of the solitary wave amplitude a and has the opposite polarity. However, we see from (32) that because V is decreasing, the wavenumber k of the trailing radiation increases. Also, although the amplitude b is independent of a, it does vary with α, δ as the wave shoals.

In contrast, when $\beta = 0$, the expression for the solitary wave amplitude continues to hold and yields the well-known expression

$$\mathcal{A} = \mathcal{A}_0, \quad \frac{a}{a_0} = \left(\frac{\alpha\delta_0}{\alpha_0\delta} \right)^{1/3}, \quad \text{and} \quad \frac{\eta}{\eta_0} = \left(\frac{\mu c^2 Q_0^2 \lambda_0}{\mu_0 c_0^2 Q^2 \lambda} \right)^{1/3}. \tag{33}$$

Also, the trailing tail is determined in a different way, as now

$$A^{(1)} \to -\frac{M_\tau^{(0)}}{V}, \quad \text{as} \quad \theta \to -\infty, \quad \text{where}$$
$$M^{(0)} = \int_{-\infty}^{\infty} A^{(0)} \, d\theta.$$

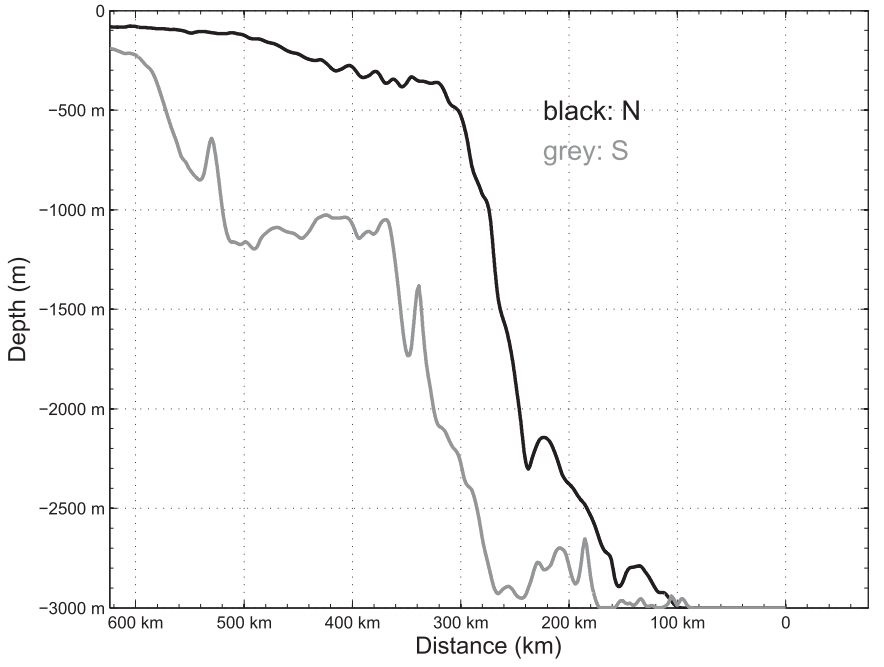

FIG. 1. Two sets of averaged topography used in the two-dimensional experiments: the northern cross section (black line; averaged between 21.4° and 21.6°N) and the southern cross section (gray line; averaged between 20° and 20.2°N).

Because $M^{(0)} = 2a/K$ is the mass of the solitary wave, this is just the expression of conservation or mass. Hence, the amplitude of the trailing tail at the solitary wave location is $A_s = A^{(1)}(\theta \to \infty)$, we find that

$$A_s = \frac{2a_\tau}{VK} = \frac{a_\tau}{4\delta K^3} = \frac{12^{1/2}\overline{\alpha}_\tau}{C_0^{1/2}\delta\overline{\alpha}^{5/3}},$$
$$\overline{\alpha} = \frac{\alpha}{\delta}, \quad \text{and} \quad C_0 = \frac{a_0}{\overline{\alpha}_0^{1/3}}. \tag{34}$$

When $\overline{\alpha}$ is decreasing, A_s *h*as the opposite polarity to the solitary wave. This can now be compared with the corresponding expression (32) when rotation is present.

2) OSTROVSKY NUMBER

By examining the integrability or otherwise of the reduced Ostrovsky equation, that is (7) with the third-order linear dispersive term omitted, Grimshaw et al. (2012) showed that rotation inhibits nonlinear steepening and hence the formation of solitary-like waves, consistent with results found numerically by Gerkema and Zimmerman (1995), Gerkema (1996), and Helfrich (2007). Adapting a suggestion by Farmer et al. (2009) and Li and Farmer (2011), Grimshaw al. (2012) defined the Ostrovsky number as

$$O_s = \frac{3|\mu|\kappa}{\gamma} \quad \text{and} \quad \kappa = \max(\eta_{0\chi\chi}) = \frac{\max(A_{0XX})}{c^2}. \tag{35}$$

If $O_s < 1$, then rotational dispersion dominates over third-order dispersion, and solitary wave formation is inhibited. But if $O_s > 1$, then an initial wave profile will steepen, and solitary waves will form. If we use the KdV solitary wave [cf. (22)] for the initial condition η_0, then

$$\kappa = -4aK^2 = -\frac{\mu a^2}{3\lambda}, \quad \text{so that} \quad O_s = \frac{\mu^2 a^2}{\lambda\gamma} = \frac{a^2}{M^2},$$
$$\text{where} \quad M = \frac{(\lambda\gamma)^{1/2}}{\mu}. \tag{36}$$

Here, it is assumed that $\mu < 0$ and so $a < 0$. The useful length scale M is derived from the Ostrovsky equation (7) by renormalizing so that all coefficients are at unity; that is, in the notation of Grimshaw and Helfrich (2008), x, t, and η are scaled by L, P, and M, respectively, where

$$L^4 = \frac{\lambda}{\gamma}, \quad P = \frac{L^3}{\lambda}, \quad \text{and} \quad M = \frac{\lambda}{\mu L^2} = \frac{(\lambda\gamma)^{1/2}}{\mu}. \tag{37}$$

For the two-layer fluid model of the SCS, see below in section 2c, and for the experiment on the Coriolis platform (see Grimshaw et al. 2013) $O_s \gg 1$, but this is a consequence of taking a KdV solitary wave as an initial profile. An alternative choice of the initial condition is the leading trailing wave seen in the numerical solutions or estimated asymptotically as above. That is, let

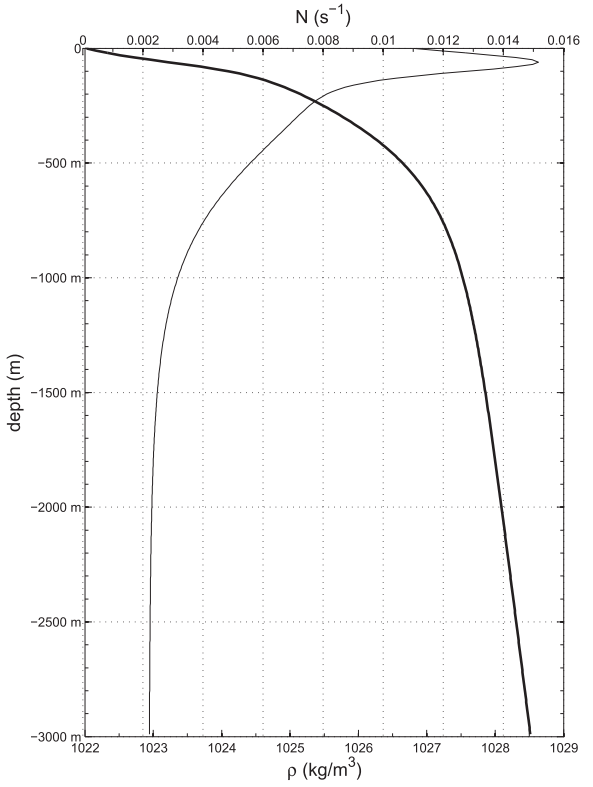

FIG. 2. Vertical profile of the background density (thick line, lower abscissa) and the buoyancy frequency (thin line, upper abscissa).

$$A^{(0)} = b\sin(kx), \tag{38}$$

where b, k are found from (31) and (32). Then, we find that

$$O_s = \frac{3|\mu b|k^2}{\gamma c^2}, \quad \text{so that} \quad O_s = \frac{36(\gamma\lambda)^{1/2}}{\mu a} = \frac{36M}{a}. \tag{39}$$

Interestingly, now O_s is inversely proportional to the initial solitary wave amplitude. Thus initially, in the SCS example $O_s = 0.9$ but in the Coriolis experiment $O_s = 3.1$, indicating that the tail formation and subsequent evolution is more important in the Coriolis experiment than in the SCS.

c. *Two-layer fluid*

Consider a two-layer fluid in which the density is a constant ρ_1 in an upper layer of height h_1 and a constant $\rho_2 > \rho_1$ in the lower layer of height $h_2 = h - h_1$. For simplicity, we shall also assume that $\rho_1 \approx \rho_2$, the usual situation in the ocean, and also then the upper boundary condition for $\phi(z)$ then becomes just $\phi(0) \approx 0$, the so-called rigid-lid approximation commonly used for internal waves. Then we find that

$$\phi = \frac{z+h}{h_2} \quad \text{for} \quad -h < z < -h_1 \quad \text{and}$$
$$\phi = -\frac{z}{h_1} \quad \text{for} \quad -h_1 < z < 0, \quad \text{and} \tag{40}$$

$$c^2 = \frac{g' h_1 h_2}{h_1 + h_2}, \quad \mu = \frac{3c(h_1 - h_2)}{2h_1 h_2},$$
$$\lambda = \frac{c h_1 h_2}{6}, \quad \text{and} \quad \gamma = \frac{f^2}{2c}. \tag{41}$$

Note that the nonlinear coefficient $\mu < 0$ for these interfacial waves when $h_1 < h_2$. It then follows that

$$L^4 = \frac{c^2 h_1 h_2}{f^2}, \quad M = \frac{f(h_1 h_2/3)^{3/2}}{c(h_1 - h_2)}, \quad \text{and}$$
$$T = \frac{1}{\gamma}\left[\frac{(h_1 - h_2)A^{(0)}}{8h_1^2 h_2^2}\right]^{1/2}.$$

For the SCS, with $f = 5 \times 10^{-5}\,\mathrm{s}^{-1}$, $h_1 = 500\,\mathrm{m}$, $h_2 = 2500\,\mathrm{m}$, $c = 2.35\,\mathrm{m\,s}^{-1}$, and then $M = 3\,\mathrm{m}$, $L = 5.5\,\mathrm{km}$, and $T = 4.6$ days; thus, for an initial amplitude of 120 m, the scaled amplitude is 40, implying a collapse to a wave packet, although for this amplitude the extinction time is $t_e = 3.4$ days. For the experimental study of Grimshaw et al. (2013), $f = 4\pi/T_p$, $T_p = 45\,\mathrm{s}$, $h_1 = 6\,\mathrm{cm}$, $h_2 = 30\,\mathrm{cm}$, $c = 7\,\mathrm{cm\,s}^{-1}$, $M = 0.77\,\mathrm{cm}$, $L = 11.7\,\mathrm{cm}$, and $T = 7.6\,\mathrm{s}$; thus, for an initial amplitude of 9 cm, the scaled amplitude is 12, consistent with the observed collapse to a wave packet; the extinction time is $t_e = 5.2\,\mathrm{s}$.

3. Numerical results for the South China Sea

We next present some typical numerical solutions of the variable coefficient Ostrovsky equation (9) and two-dimensional simulations using the MITgcm (Marshall et al. 1997) for stratification, topography, and initial solitary waves that are representative of the conditions in the SCS. The SCS is a region where ISWs, generated by tidal flows in the Luzon Strait, propagate westward from the Luzon region toward the Chinese continental shelf (Zhao and Alford 2006; Alford et al. 2010). It takes about 2 days for waves to propagate across the SCS and onto the continental shelf. Thus, the effects of rotation may become significant in the shoaling process, providing an interesting and realistic setting to explore the role of rotation on ISW shoaling. The Ostrovsky equation solutions have the advantage of being closely connected to the theoretical development above, while the MITgcm simulations allow the exploration of effects, such as strong nonlinearity and interactions of vertical modes, not accounted for in either the theory or the solutions of the Ostrovsky equation.

Two cross sections with averaged topography, the northern cross section (averaged between 21.4° and 21.6°N) and the southern cross section (averaged between 20° and 20.2°N), are shown in Fig. 1. The topography is obtained from the 1-min gridded elevations/bathymetry for the world (ETOPO1) Global Relief Model dataset (Amante and Eakins 2009). These two cross sections are representative of the topography in this area: the northern one features a drastic change of slope, whereas the southern one is similarly steep in the deep part, but the shelf break is much deeper (1000 m). It features a smooth change of topography, followed by a second slope and shelf break. The southern cross section is overall deeper than the northern one. The background stratification used in the simulations is derived from the summer climatological *World Ocean Atlas 2005* (Boyer et al. 2006) (Fig. 2). The stratification is taken to be spatially uniform and ambient flows are not included.

Both models are initialized with a single, first-mode ISW with amplitudes of 60–90 m propagating westward from the deep basin east of the slope. This is consistent with in situ observations (Alford et al. 2010) and satellite images that frequently show isolated, westward-propagating ISWs with comparable amplitudes in the deep basin west of the Luzon Strait (Zhao et al. 2004). The wave evolution is then followed up the slope onto the shelf.

a. Ostrovsky equation simulations

The variable coefficient Ostrovsky equation (12) is solved using a Fourier pseudospectral method, with dealiasing for the nonlinear terms in the time-like phase variable X and a fourth-order Runge–Kutta technique for integration in the evolution variable T. The calculations use a periodic domain in x that varies between runs, but is large enough to avoid significant issues associated with the wraparound of the evolving wave solution. The numerical resolution varies between runs, but was on the order of $\Delta T = 100$ s and $\Delta X = 10$–100 m.

All of the Ostrovsky equation simulations presented here include a cubic nonlinear term $\mu_1\eta^2\eta_x$ in (9) because this term generally improves the agreement of KdV-class models with observations and more complete models such as the MITgcm [see Holloway et al. (1999, 2001), Grimshaw (2001), and Helfrich and Melville (2006) for instance]. Like the other coefficients of (9), μ_1 is a function of $\rho_0(z)$, $\mu_0(z)$, c, and the eigenfunction $\phi(z)$. It also depends on a nonlinear correction to ϕ. See Holloway et al. (1999) and Grimshaw et al. (2004) for the details on determining μ_1. [Note that the definition of μ_1 in (5) of Grimshaw et al. (2004) is missing a factor of 2 in the denominator.]

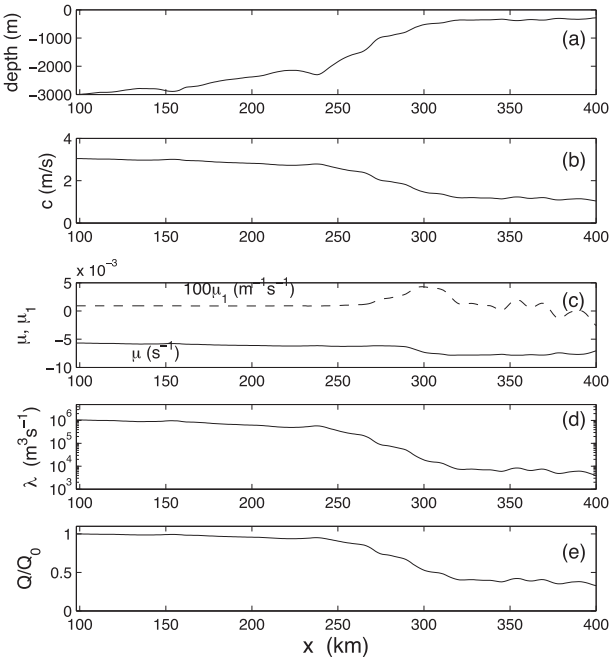

FIG. 3. Coefficients of the Ostrovsky equation for the northern topography section of the South China Sea. (a) Northern section topography; (b) c; (c) μ and μ_1; (d) λ; and (e) Q/Q_0.

The coefficients of (9) are functions of x, and hence vary with T in the transformed (12). Figure 3 shows the dimensional values of the coefficients and the linear phase speed c computed using the stratification in Fig. 2 and the topography of the northern section of Fig. 1. The rotational coefficient $\gamma = f^2/2c$ is not shown, but can be found from c and the Coriolis frequency $f = 5.066 \times 10^{-5}\,\mathrm{s}^{-1}$. The value of Q in (10) at $x = 0$ is indicated by Q_0. The plot only shows $x > 100$ km as the coefficients are constant in the uniform depth of the basin. Further note that μ is negative for all $x < 400$ km, and so a turning point is not encountered and the KdV solitary waves are waves of depression in this range of x. The coefficient of the cubic term μ_1 is positive over most of the domain and much smaller than μ. For waves of amplitude $\eta_0 = -80$ m, the ratio of the cubic to quadratic terms $|\mu_1\eta_0/\mu| \sim 0.1$ for $x < 400$ km. As a consequence, the effects of cubic nonlinearity are expected to be quite small. This is borne out by the comparison of calculations with and without the cubic term that show only minor quantitative differences.

Figure 4 shows a solution for an initial solitary wave with amplitude $\eta_0 = -64$ m released in the deep basin at $x_0 = 54$ km with $t = 0$ at the wave crest. In this example the rotation has been set to zero, $\gamma = 0$. The figure shows the time series of wave amplitude η at selected locations in the range $205 \le x \le 380$ km. It is not until $x > 250$ km,

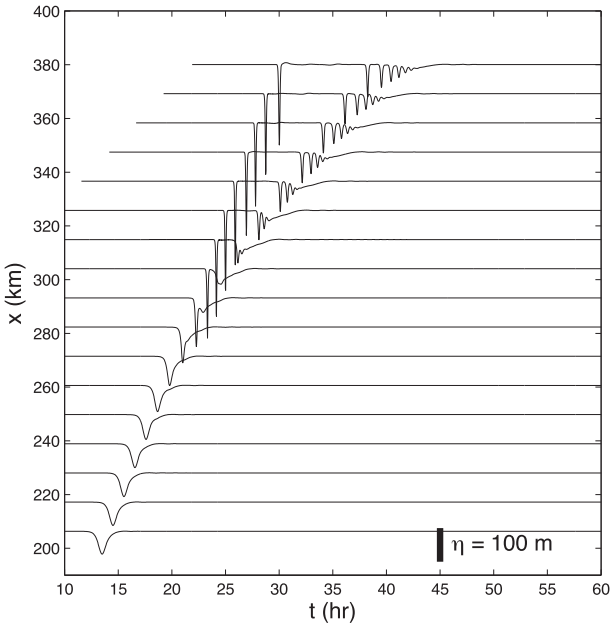

FIG. 4. Numerical solution of the variable coefficient Ostrovsky equation (12) for the northern topography with no rotational effects ($\gamma = 0$). The initial wave has amplitude $\eta_0 = -64$ m at $x_0 = 54$ km. Time series of wave amplitude $\eta(x, t)$ at selected x locations on the slope are shown. The scale on the lower right indicates wave amplitude.

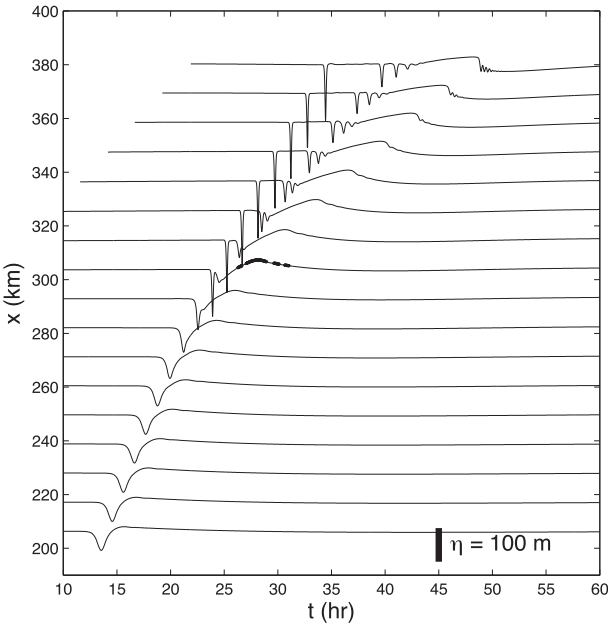

FIG. 5. As in Fig. 4, but with rotation included. The heavy line segments in the η time series at $x = 304$ km indicate regions of the trailing waves where $O_s > 1$.

where the total depth is less than 1000 m and the coefficients in Fig. 3 begin to change significantly, that the incident wave shows significant effects of the topography. As it propagates up the slope, it undergoes a fissioning process. The leading solitary wave separates from a trailing wave packet; the leading wave propagates adiabatically with the local solitary wave speed $c + \alpha a/3$, where a is the local amplitude [see (22) and (23)], and the trailing tail will initially have the speed c, until steepening and fissioning occur; then the leading wave of the trailing tail will have the local solitary speed. The initial shoaling process does produce a trailing tail as discussed above, but it is quite small and obscured by the fissioning.

In contrast, the inclusion of rotational effects ($\gamma \neq 0$) produces the wave evolution shown in Fig. 5. The incident solitary wave still undergoes a fissioning process similar to that shown in Fig. 4, although the number of the scattered waves has decreased and the waves are smaller (by a factor $\approx \frac{2}{3}$) with rotation included. The energy in the initial wave is lost to a larger amplitude trailing wave as discussed in section 2b. This trailing wave grows as it propagates up the slope and eventually steepens to produce a secondary wave packet located at $x = 380$ km at $t = 50$ h. This striking new feature, which as far as we are aware has not previously been reported, is due to a combination of rotation and topography. Rotation has had the effect of enhancing the trailing wave to a point where it steepens sufficiently to produce a KdV-like undular bore. The heavy line segments in the time series at $x = 304$ km indicate regions of the trailing wave where the Ostrovsky number (35) $O_s > 1$. Recall that in the absence of nonhydrostatic dispersion and cubic nonlinearity ($\lambda = \mu_1 = 0$) and constant μ and γ, regions of $O_s > 1$ indicate that breaking, and solitary waves, will occur. Because the numerical solution has finite λ and μ_1 and variable coefficients, the Ostrovsky number criterion may not be directly applicable. However, the presence of a region of $O_s > 1$ is an indicator that solitary waves may emerge from the trailing wave, as they eventually do.

The formation of the trailing wave takes a finite evolution time (or alternatively evolution distance) and thus the processes shown in Fig. 5 should depend on the location x_0 at which the incident wave is initiated. Figure 6 shows a time series at $x = 380$ km for a run with $\eta_0 = -64$ m, but now initiated at $x_0 = 136$ km (the lower curve). The phase of this solution has been shifted so that the trailing wave arrives at approximately the same time as the $x_0 = 54$-km case (also shown as the middle curve in the figure). The amplitude of the trailing tail $\eta_s \approx 20$ m is slightly less than the $x_0 = 54$-km case, where $\eta_s \approx 22$ m and the packet has only just begun to emerge. Recall that the amplitude of the trailing wave is predicted to be independent of the initial solitary wave amplitude η_0. However, the wavenumber of the trailing

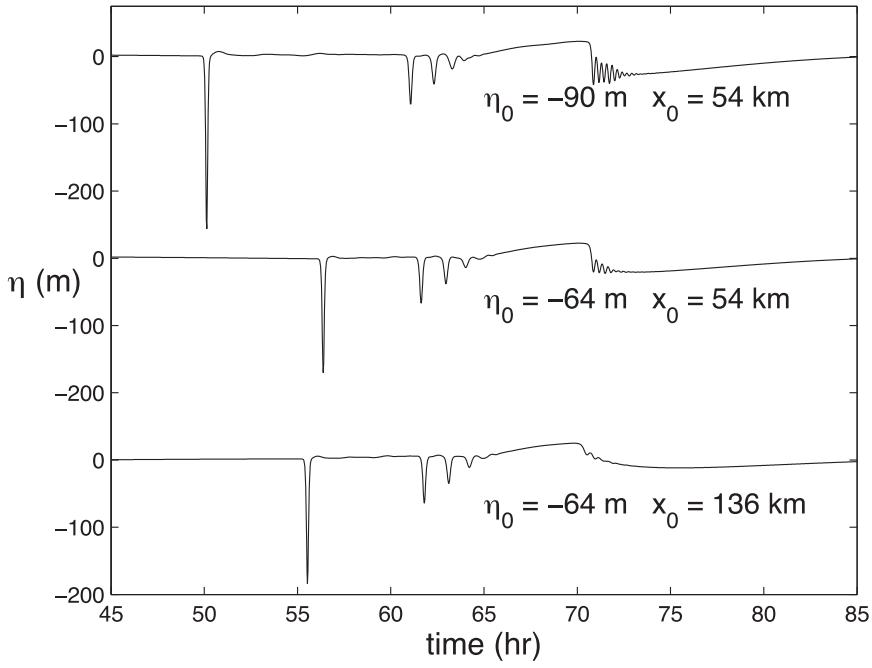

FIG. 6. Time series of Ostrovsky equation (12) solutions for the northern topography at $x = 380$ km for a solitary wave with amplitude η_0 and initial location x_0 as indicated.

wave and the rate at which it is produced [see the extinction time (29)] does depend on η_0. Thus, the evolution of the trailing packet should depend on η_0. The top curve in Fig. 6 shows a time series η at $x = 380$ km for a run with a larger initial solitary wave, $\eta_0 = -90$ m initiated at $x_0 = 54$ km. The amplitude of the trailing tail $\eta_s \approx 22$ m is almost the same as the $\eta_0 = -64$-m case; however, the dispersive packet is more developed for the larger initial wave, and the leading solitary wave is substantially larger.

The calculations shown here agree qualitatively with the predictions of the theoretical development for the Ostrovsky equation. Rotation produces a trailing inertia–gravity wave with an amplitude that is independent of the initial solitary wave amplitude. This trailing wave possesses regions where $O_s > 1$ and subsequently steepen to form a trailing wave packet, which is absent in the nonrotating case. However, note that in these calculations the leading solitary waves on the shelf at $x = 380$ km have amplitudes $-\eta \approx 150$–250 m in water depths of ≈ 300 m. These are unrealistically large waves and well beyond the applicability of the weakly nonlinear assumption inherent in the Ostrovsky equation. There are several possible explanations for these large amplitudes including the absence of dissipation and the restriction of the model to a single vertical mode. Furthermore, on the shelf the coefficient of the cubic term $\mu_1 > 0$, albeit quite small. In this situation solitary wave solutions of the KdV equation with cubic nonlinearity do not have a limiting wave amplitude when $\mu\eta_0 > 0$, where η_0 is now the local solitary wave amplitude (Grimshaw 2001). Thus, the simulations can develop unrealistically large waves when compared to fully nonlinear theories or models. These limitations suggest exploration of the effects of rotation on shoaling using the more complete physics in the MITgcm as discussed in the next section.

b. MITgcm simulations

1) MODEL DESCRIPTION

In this section, we describe simulations using a two-dimensional version of the MITgcm (Marshall et al. 1997). The horizontal resolution is 250 m, with telescoping grids implemented in the open boundaries, and 180 layers are used in the vertical direction, with a resolution of 10 m in the upper 1500 m and of 50 m in the lower 1500 m. The time step is 12.5 s. Given the possibility of strong wave breaking and mixing near the shelf break, a Richardson number–dependent scheme (see Pacanowski and Philander 1981) was used to parameterize the vertical viscosity and diffusivity. The horizontal viscosity was calculated with the Leith scheme (see Leith 1996). Sensitivity experiments on the implementation of these two schemes were performed, and these showed that the essential features

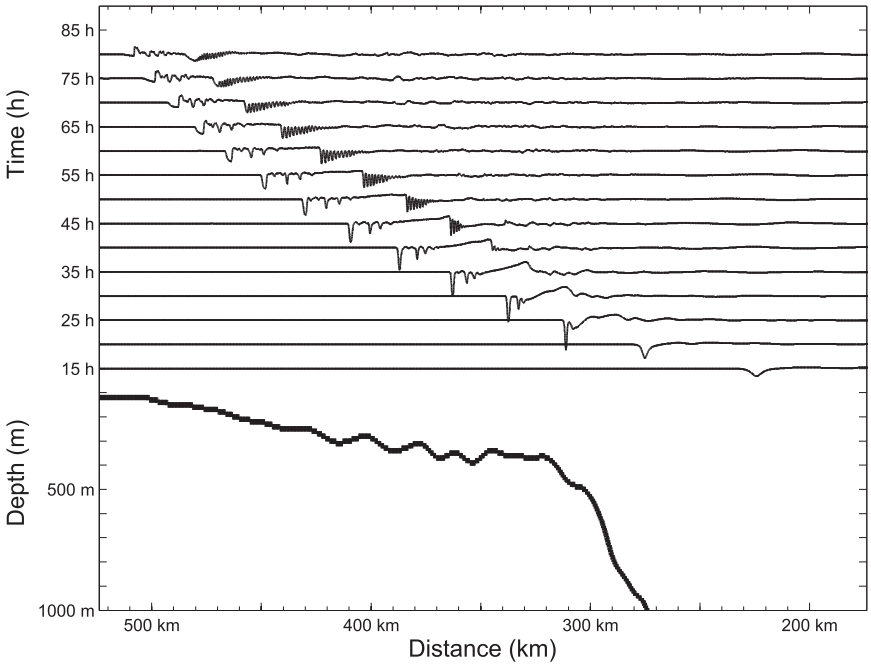

FIG. 7. Two-dimensional evolution of an ISW with amplitude of 90 m under the effects of rotation along the northern cross section. The isopycnal of $\rho = 1024\,\mathrm{kg\,m^{-3}}$, which is located at 100 m when at rest, is shown at an equal time interval of 5 h. The shown isopycnals start at $t =$ 15 h when the ISW approaches the shelf break. The lowest thick line is the topography in the upper 1000 m, with the 0-m depth at the position of 15 h. The y axis for the topography also measures the scale of the displacement of the plotted isopycnals.

remained identical, but numerical noise arose without these two schemes.

As with the Ostrovsky equation solutions, the simulations are started with a single, westward-propagating solitary wave in the deep basin. However, a complicated step of the model initialization here was the setting up of the initial incoming wave. First, in a two-dimensional configuration with constant depth of 3000 m, a KdV solution for a first-mode depression wave was substituted into the MITgcm, which then evolves toward a new steady state. After becoming fully detached from the structures behind it, this newborn ISW was truncated and then used as an initial condition for the shoaling experiments.

2) MODEL RESULTS

Figure 7 shows the evolution of the shoaling wave. Overall the evolution is similar to that for the Ostrovsky equation shown in Fig. 5. Here, as in the analogous Ostrovsky equation simulation, the striking new feature is the formation of a secondary wave train. The leading ISW is progressively shaped by the changing environment, with a decreasing amplitude and commencement of wave fission. Note also that this incoming ISW from deep water experiences severe further deformation when passing through the shelf break, with the radiation of the secondary waves. The distances between the fissioned ISWs are enlarged due to nonlinear dispersion. The broadening and subsequent polarity reversal of the leading ISW occur after $t = 60$ h when the leading wave is located above the depth of about 130 m.

As already mentioned above, the most interesting finding of these simulations is the generation of a secondary nonlinear wave train, which is due to the joint effect of rotation and topography. According to Fig. 7, accompanying the reshaping of the leading ISW near the shelf break ($t = 25$ h), behind it the isopycnal is elevated, quickly steepens, and disintegrates into a nonlinear wave train with an increasing number of waves. The first wave of this wave train also broadens and exhibits a scenario of polarity reversal when further traveling up into the shallow water. Behind the wave train are some higher modes that are generated due to either scattering by the topography or nonlinear scattering of wave energy.

To further test and verify this joint role of rotation and shoaling over topography, the same experiment but without rotation was performed, and the results are shown in Fig. 8. It is seen that, at $t = 25$ h, an elevation also emerges behind the incoming ISW, and it is just as strong as that in Fig. 7 at the same moment of time. However, unlike the rotational case, this elevation does

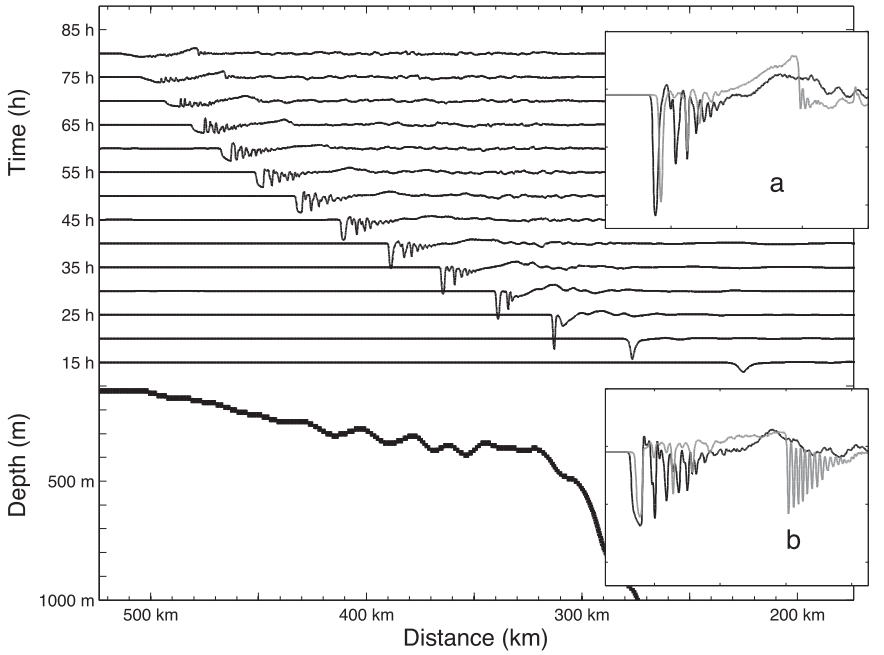

FIG. 8. As in Fig. 7, but for the rotation switched off. The two insets display the comparison of the isopycnals with (gray) and without (black) rotation at $t = 40$ h (inset a) and 55 h (inset b).

not transform into a wave train. Instead, it becomes increasingly smoother until it reaches the very shallow water where it reveals a slight tendency to steepen at $t =$ 75 h. Meanwhile, the initial incoming ISW goes through a similar transformation process, but with a larger wave amplitude and more fissioned waves. This is because less energy is shed backward from the initial ISW when compared to the rotational case. The larger leading ISW packet in the nonrotational case "feels" the bottom and goes through wave polarity reversal at an earlier stage, which leads to the production of a fissioned leading ISW packet with larger amplitudes and more waves. A comparison of two scenarios at $t = 40$ and 55 h with and without rotation is shown in the two insets of Fig. 8, and the contrast is immediately apparent. The conclusion that can be drawn from this comparison is that it is rotation that engenders the formation of the secondary wave train. Thus, as in the Ostrovsky equation simulations, the combined effect of shoaling over topography and rotation leads to the emergence of secondary wave packets, which contrasts with previous studies on ISW evolution that typically found only one wave packet in the shoaling process.

A similar scenario is shown in Fig. 9 for the southern cross section. However, in this case the main shelf break is deeper and is situated nearly 200 km west of the shelf break of the northern cross section. As a result, the secondary wave train emerges much later and farther west in this area. Also, the wave train is less significant than that in the northern cross section. Compared with the nonrotational case, one can see that without rotation (insets in Fig. 9) the secondary wave train does not appear and the initial ISW is larger at all stages.

3) SOLUTION PROPERTIES FOR A RANGE OF ENVIRONMENTAL PARAMETERS

In this section, we explore the combined effect of rotation and shoaling over topography in a series of sensitivity simulations in which the topography and rotation are independently varied. All these simulation were initialized with an ISW of amplitude 64 m released at $x =$ 52.5 km. Figure 10 shows a family of four model topographic slopes based on the actual northern and southern cross sections of the SCS used above. All have the same depth at the shelf break. The corresponding model simulations for an initial wave with an amplitude of 64 m are shown in Fig. 11. The figure shows the displacement of the 1024 kg m^{-3} isopycnal of the waves on the shelf. Decreasing the slope decreases the fissioning of the primary wave because it has more time to adjust adiabatically to the depth change, consistent with nonrotating KdV theory and modeling (Grimshaw et al. 2004, 2010). The decrease in slope also results in an increase in the number of trailing packets associated with the rotation, as evident for $\alpha = 0.1°$ where two packets have developed. This is again consistent with ideas of ISW decay by

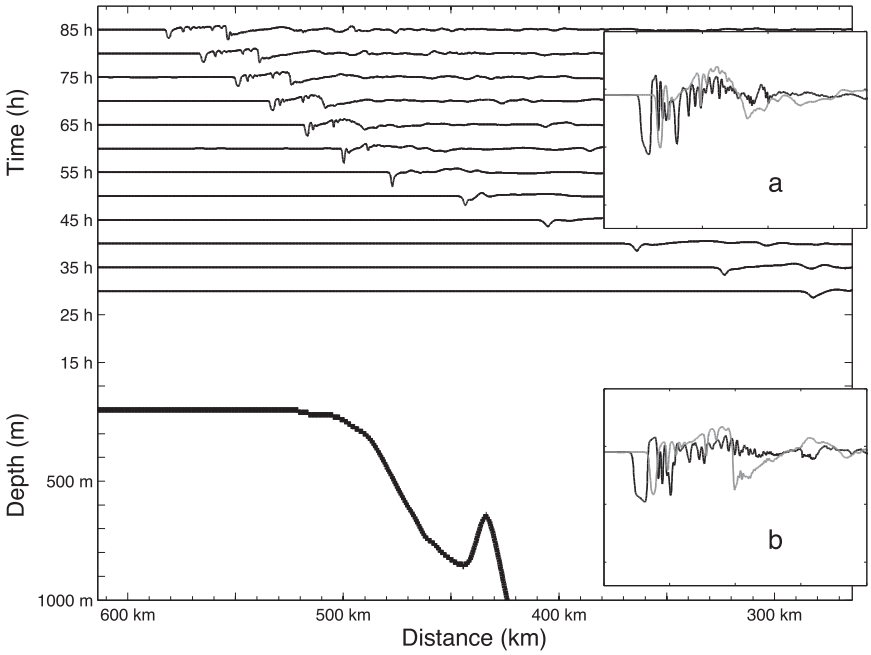

FIG. 9. As in Fig. 7, but for the southern cross section. The two insets display the comparison of the isopycnals with (gray) and without (black) rotation at $t = 65$ h (inset a) and 75 h (inset b).

inertia–gravity wave radiation discussed in section 2b (1). The longer propagation distance over the slope leads to a longer trailing inertia–gravity wave packet (with an approximately constant wavenumber). The increase in inertia–gravity wave crests produces more of these short, solitary wave packets. However, these packets are weaker than the packets produced for the steeper slopes.

Figure 12 shows a family of four model topographic profiles with the same continental slope ($\alpha = 1.63°$), but different depths at the shelf break; here, the rotation rate is fixed at f_0. The corresponding model simulations

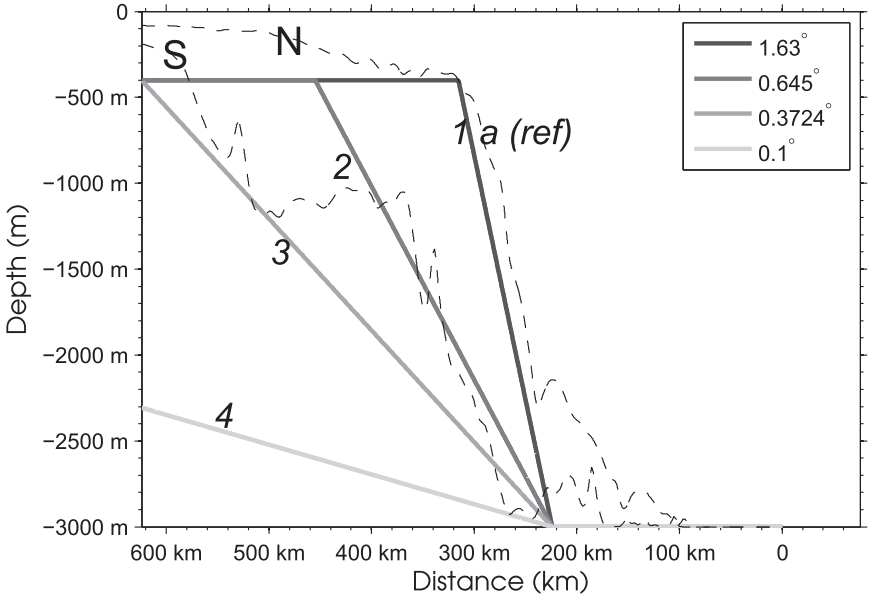

FIG. 10. Model topographies for the sensitivity simulations. All four cases have the same depth on the shelf $H_{\text{shelf}} = 400$ m. The shelf breaks of topographies 1–4 are located at 315.4, 455, 624, and 1724 km, respectively.

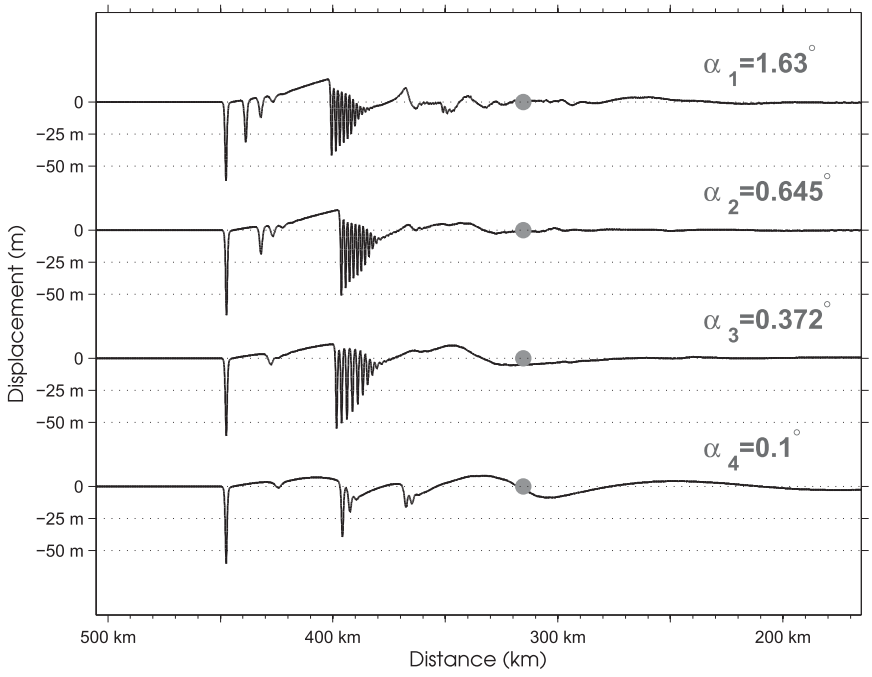

FIG. 11. A comparison of model results with the topographic slopes shown in Fig. 10. The isopycnal 1024 kg m^{-3} is drawn in the figure. Note that the x axis is for the reference slope. The distance for the three weaker slopes has been offset for comparison. Thus, each case is at a different time. The gray dots indicate the positions of the shelf break for the individual topographies. The amplitude of the incident solitary wave is 64 m in all simulations and the rotation rate f_0 corresponds to that in the northern SCS.

are shown in Fig. 13. First, decreasing the depth on the shelf from the reference case of H_{shelf} = 400–200 m reduces the amplitude and fissioning of the primary wave. The trailing rotation-induced wave packet persists. There is no noticeable wave breaking in this experiment; instead, wave energy scattering into higher modes is more pronounced, and there is a very clear reflected wave due to the tall and steep topography in this case [both the higher modes and the reflected wave can be clearly seen from the full two-dimensional density fields (figure not shown here); for the scenario of higher modes, see also Fig. 15, described in greater detail below]. Increasing the shelf depth eliminates the trailing packet, although the trailing inertia–gravity wave tail is apparent. One possible interpretation is that the Ostrovsky number (35), $O_s = 3\mu\kappa/\gamma$, in the trailing tail is decreasing as the shelf depth is decreased. Figure 13 shows that the curvature κ does decrease for H_{shelf} = 700–1000 m because of the decreased effects of steepening due to the shoaling of the trailing inertia–gravity wave. This overcomes an increase ≈ 1.3 in μ/γ (from Fig. 3) on the shelf for H_{shelf} = 1000 m.

Finally, Fig. 14 shows a set of simulations as the rotation increases from 0 to 4 times the Coriolis frequency f_0 of the northern section of the SCS. The runs all use the reference topographic profile with $\alpha = 1.63°$ and H_{shelf} = 400 m in Fig. 10 and an initial wave of 64 m. Increasing the Coriolis frequency from zero to f_0 promotes the formation of the trailing undular bore as expected from the earlier discussion. However, a further increase of f then strongly modifies the resulting evolution. For $f = 2f_0$, the increased rotation has rapidly extinguished the initial solitary wave. This gives rise to a weak leading wave on the shelf and a trailing undular bore that has more time to disperse in place of the waves produced by the fissioning for lower rotation. A weaker, second wave packet is emerging behind this first group. For $f = 4f_0$, the rotation rapidly eliminates the initial solitary wave and produces a leading nonlinear inertia–gravity packet of the type found in long time solutions of the Ostrovsky and related equations for constant depth (Helfrich 2007; Grimshaw and Helfrich 2008). In this case, the connection to the theory in section 2 is tenuous as rotation dominates the initial evolution.

The same qualitative sensitivity to topography and rotation just described for the MITgcm simulations is found in numerical solutions of the Ostrovsky equation (not shown here). However, because of the limitation of the Ostrovsky equation to a single vertical mode, weak nonlinearity, and no dissipation, there are some

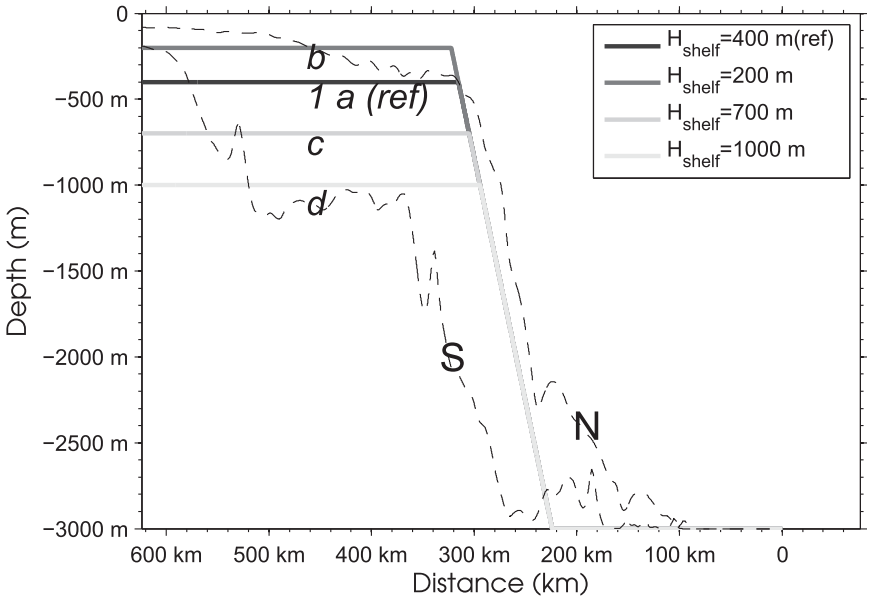

FIG. 12. Model topographies with variations in the depth at the shelf break H_{shelf}. All have a slope of $\alpha = 1.63°$.

substantial differences. In this context, one very interesting feature is the emergence of a second-mode breather in the MITgcm runs. This is best seen in a movie animation for the simulation shown in Fig. 7, and here we show in Fig. 15 a snapshot at $t = 44$ h from that movie. The two-mode structure is clearly evident, and the movie shows the unsteady wave packet structure. As time progresses the isopycnal displacements

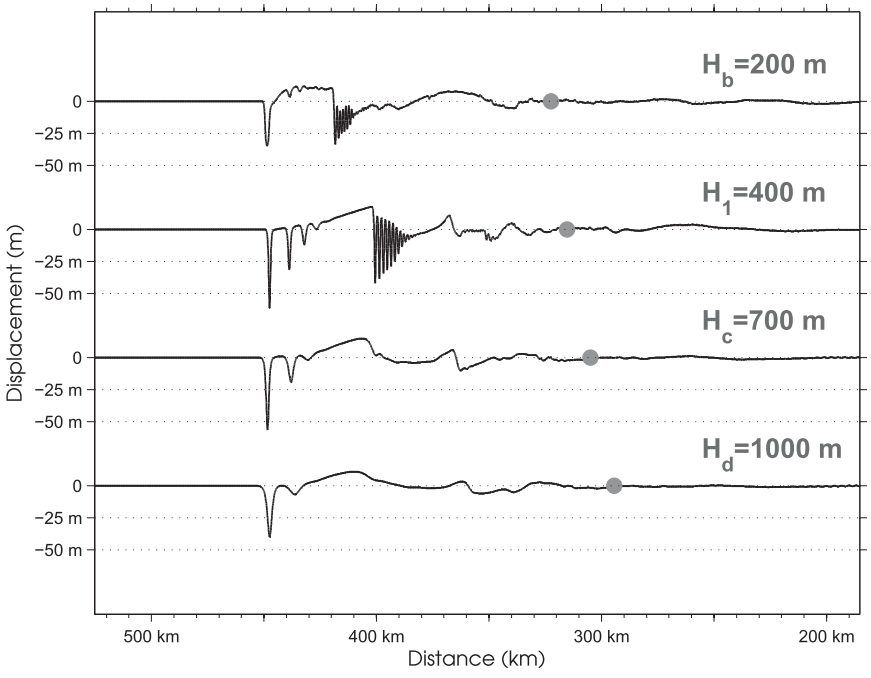

FIG. 13. A comparison of model results with topographic slopes with different depths at the shelf break. The isopycnal 1024 kg m^{-3} is drawn in the figure. The gray dots indicate the positions of the shelf break for the individual topographies. The initial amplitude is 64 m. The outputs are at different moments of time.

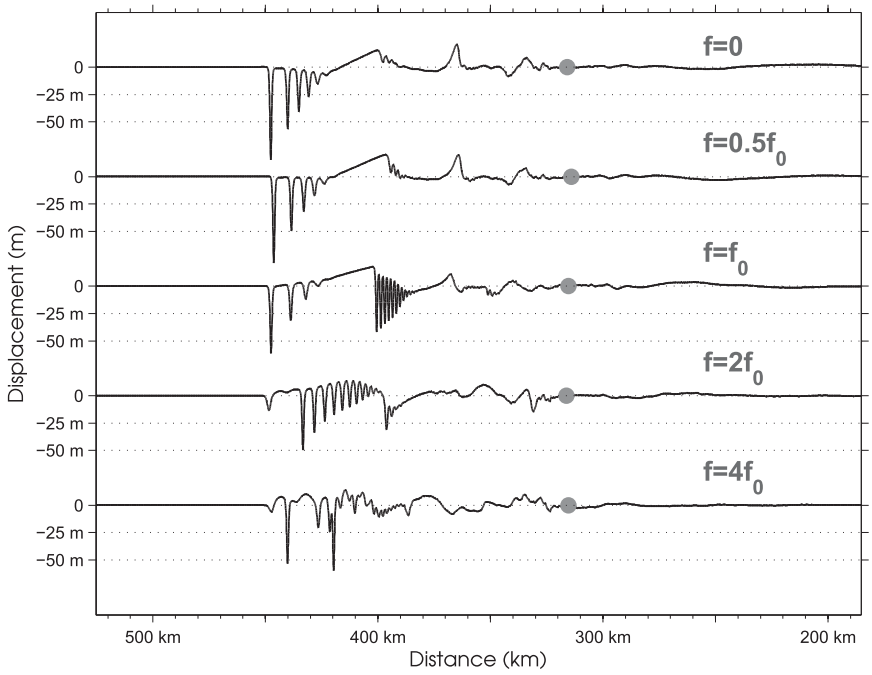

FIG. 14. A comparison of model results with different strengths of rotation (0, 0.5, 1, 2, and 4) f_0. The displacement of the 1024 kg m^{-3} isopycnal is shown. The gray dots indicate the positions of the shelf break for the individual topographies. The initial solitary wave amplitude is 64 m. The topography is the same for the runs (topography 1 in Fig. 10), and the outputs are at different moments of time.

within the packet oscillate periodically from elevation to depression, and vice versa, while the envelope of the packet propagates steadily. One caveat to this identification of a breather is that the product of the second-mode cubic nonlinear and dispersive coefficients of the KdV equation $\mu_1\lambda < 0$ in the region where the breather is found. Formally, breathers only exist for a positive product (see Pelinovsky and Grimshaw 1997; Grimshaw et al. 2001). However, the numerical solution is fully nonlinear and includes rotation effects that are not considered in the theory and may contribute to the numerical observation. There have been several previous reports of a second-mode disturbance [see Vlasenko and Hutter (2001), Vlasenko and Alpers (2005), and sections 5.4.3 and 6.4 of the monograph by Vlasenko et al. (2005), for instance], excited by interaction of a first-mode ISW with topography, but this would seem to be the first identification of such a disturbance as a breather where background rotation is involved.

4. Discussion and conclusions

While the deformation due to the shoaling of an ISW has been heavily studied and documented [see the recent review by Grimshaw et al. (2010)] and the effect of Earth's background rotation on an ISW in a uniform environment has been separately studied, most recently by Grimshaw and Helfrich (2008, 2012) and Grimshaw et al. (2013), their joint effects have not previously been investigated in detail. This is the aim in this paper, and we have approached this task in two complementary ways. First, we have presented a variable coefficient Ostrovsky equation (9) as a basis to develop some theoretical analysis and as a suitable relatively simple model for numerical simulations. This equation combines the well-known variable coefficient KdV equation with the Ostrovsky equation, which is the extension of the KdV equation to incorporate the effects of rotation. Second, we have used the MITgcm in a two-dimensional configuration to simulate the passage of an ISW across a certain cross section of the SCS.

Our main finding is that rotation induces the formation of a secondary wave packet, trailing behind the leading wave, and with the structure of a KdV-like undular bore. The key to understanding this feature is the generation of a trailing tail by the leading wave as it shoals under the influence of the background rotation. Shoaling alone will induce the formation of a trailing tail, but for the simulations reported here this does not develop further into an undular bore. The effect of the

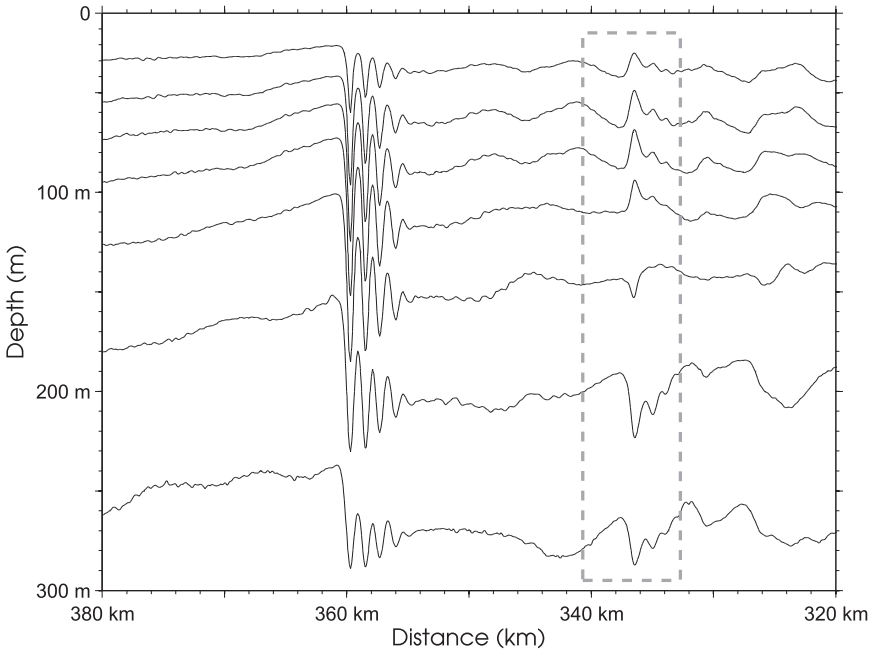

FIG. 15. A snapshot at $t = 44$ h of the simulation shown in Fig. 7. The single isopycnal of $\rho = 1024\,\mathrm{kg\,m^{-3}}$, located at 100 m when at rest, is here embedded in a family of seven neighboring isopycnals. The dotted box indicates the location of the breather.

background rotation enhances the trailing tail sufficiently for it to steepen and then break with the consequent formation of an ISW wave train, that is, an undular bore. As the system parameters (i.e., the topographic slope and the background rotation) are varied, we have found that this is a robust phenomenon, although the details of the bore structure, such as its amplitude and number of undulations, are sensitive to the parameter values.

While the present results are confined to the topography and density stratification of the chosen cross section of the SCS, with the variations described in the sensitivity tests of section 3b(3), these are rather typical for many continental slopes and shelves. That is, the density stratification is two-layer like, and the topographic slope is essentially monotone, rising from a deep basin to a shallow shelf. Although the SCS is somewhat unique because the long propagation distance across the basin increases the time for rotation to become significant, we still expect that the development of secondary trailing wave packets, similar to those found here, will be observed in many other locations. We emphasize that the complicated structure of the internal waves over the slope, seen in Fig. 7 for instance, is the outcome of just a single incident ISW onto the continental slope. This implies that the identification of the origin of internal waves observed in coastal waters can be a quite difficult and complicated task and in general needs supporting simulations such as those reported here to reach a correct interpretation. The SCS observations presented in Alford et al. (2010) would seem ideal observations in which to look for the processes discussed here. Indeed, the fission of the primary shoaling solitary wave on the slope is evident. Their Figs. 3 and 4 show isolated, incident solitary waves separated by approximately 10–12 h, due to the tidal forcing, at the offshore N1 (depth of 2494 m) mooring. Farther inshore at the LR1 and LR3 moorings (depths of 609 and 331 m and distances from N1 of 130 and 176 km, respectively), the waves usually have split into rank-ordered groups. There is no clear indication of the trailing undular bore. However, the ≈12-h separation between the primary incident waves may well obscure the identification of the trailing undular bore. In the numerical simulations shown in Figs. 5 and 7, the undular bore trails the primary wave on the shelf by 10–15 h and would then coincide with shoaling solitary waves produced on the subsequent M_2 tide (or the beating of the diurnal and semidiurnal tide as occurs in the SCS). Additional numerical work that replicates more precisely the SCS observations discussed in Alford et al. (2010) is necessary to resolve this issue.

Finally, we note that the system parameters used here do not allow for a polarity reversal, that is, a change of sign of the nonlinear coefficient μ in (9); such a sign change occurs for depths less than 130 m, and this range is not shown here. This alone can cause a substantial deformation and disintegration of an ISW [see Grimshaw

et al. (2010), for instance]. How rotation might affect that situation is an interesting topic for future study.

Acknowledgments. KH was supported by Grants N00014-09-10227 and N00014-11-0701 from the Office of Naval Research.

REFERENCES

Alford, M., R.-C. Lien, H. Simmons, J. Klymak, S. Ramp, Y. J. Tang, D. Tang, and M.-H. Chang, 2010: Speed and evolution of nonlinear internal waves transiting the South China Sea. *J. Phys. Oceanogr.,* **40,** 1338–1355, doi:10.1175/2010JPO4388.1.

Alias, A., R. H. J. Grimshaw, and K. R. Khusnutdinova, 2013: On strongly interacting internal waves in a rotating ocean and coupled Ostrovsky equations. *Chaos,* **23,** 023121, doi:10.1063/1.4808249.

Amante, C., and B. W. Eakins, 2009: ETOPO1 1 arc-minute global relief model: Procedures, data sources and analysis. NOAA Tech. Memo. NESDIS NGDC-24, 25 pp.

Boyer, T., and Coauthors, 2006: *World Ocean Database 2005.* S. Levitus, Ed., NOAA Atlas NESDIS 60, 182 pp.

Farmer, D., Q. Li, and J.-H. Park, 2009: Internal wave observations in the South China Sea: The role of rotation and non-linearity. *Atmos.–Ocean,* **47,** 267–280, doi:10.3137/OC313.2009.

Gerkema, T., 1996: A unified model for the generation and fission of internal tides in a rotating ocean. *J. Mar. Res.,* **54,** 421–450, doi:10.1357/0022240963213574.

——, and J. T. F. Zimmerman, 1995: Generation of nonlinear internal tides and solitary waves. *J. Phys. Oceanogr.,* **25,** 1081–1094, doi:10.1175/1520-0485(1995)025<1081:GONITA>2.0.CO;2.

Grimshaw, R., 1981: Evolution equations for long nonlinear internal waves in stratified shear flows. *Stud. Appl. Math.,* **65,** 159–188.

——, 1985: Evolution equations for weakly nonlinear, long internal waves in a rotating fluid. *Stud. Appl. Math.,* **73,** 1–33.

——, 2001: Internal solitary waves. *Environmental Stratified Flows,* R. Grimshaw, Ed., Kluwer, 1–27.

——, 2013: Models for nonlinear long internal waves in a rotating fluid. *Fundam. Appl. Hydrophys.,* **6,** 4–13.

——, and H. Mitsudera, 1993: Slowly-varying solitary wave solutions of the perturbed Korteweg–de Vries equation revisited. *Stud. Appl. Math.,* **90,** 75–86.

——, and K. R. Helfrich, 2008: Long-time solutions of the Ostrovsky equation. *Stud. Appl. Math.,* **121,** 71–88, doi:10.1111/j.1467-9590.2008.00412.x.

——, and ——, 2012: The effect of rotation on internal solitary waves. *IMA J. Appl. Math.,* **77,** 326–339, doi:10.1093/imamat/hxs024.

Grimshaw, R. H. J., J.-M. He, and L. A. Ostrovsky, 1998a: Terminal damping of a solitary wave due to radiation in rotational systems. *Stud. Appl. Math.,* **101,** 197–210, doi:10.1111/1467-9590.00090.

——, L. A. Ostrovsky, V. I. Shrira, and Y. A. Stepanyants, 1998b: Long nonlinear surface and internal gravity waves in a rotating ocean. *Surv. Geophys.,* **19,** 289–338, doi:10.1023/A:1006587919935.

——, D. Pelinovsky, E. Pelinovsky, and T. Talipova, 2001: Wave group dynamics in weakly nonlinear long-wave models. *Physica D,* **159,** 35–57, doi:10.1016/S0167-2789(01)00333-5.

——, E. Pelinovsky, T. Talipova, and A. Kurkin, 2004: Simulation of the transformation of internal solitary waves on oceanic shelves. *J. Phys. Oceanogr.,* **34,** 2774–2791, doi:10.1175/JPO2652.1.

——, ——, ——, and ——, 2010: Internal solitary waves: Propagation, deformation and disintegration. *Nonlinear Processes Geophys.,* **17,** 633–649, doi:10.5194/npg-17-633-2010.

——, K. Helfrich, and E. Johnson, 2012: The reduced Ostrovsky equation: Integrability and breaking. *Stud. Appl. Math.,* **129,** 414–436, doi:10.1111/j.1467-9590.2012.00560.x.

——, ——, and ——, 2013: Experimental study of the effect of rotation on nonlinear internal waves. *Phys. Fluids,* **25,** 056602, doi:10.1063/1.4805092.

Helfrich, K. R., 2007: Decay and return of internal solitary waves with rotation. *Phys. Fluids.,* **19,** 026601, doi:10.1063/1.2472509.

——, and W. K. Melville, 2006: Long nonlinear internal waves. *Annu. Rev. Fluid Mech.,* **38,** 395–425, doi:10.1146/annurev.fluid.38.050304.092129.

Holloway, P., E. Pelinovsky, and T. Talipova, 1999: A generalized Korteweg–de Vries model of internal tide transformation in the coastal ocean. *J. Geophys. Res.,* **104** (C8), 18 333–18 350, doi:10.1029/1999JC900144.

——, ——, and ——, 2001: Internal tide transformation and oceanic internal solitary waves. *Environmental Stratified Flows,* R. Grimshaw, Ed., Kluwer, 31–60.

Jackson, C., 2004: An atlas of internal solitary-like waves and their properties. 2nd ed. Global Ocean Associates Tech. Rep., 559 pp. [Available online at http://www.internalwaveatlas.com/Atlas2_index.html.]

Johnson, R. S., 1973: On the development of a solitary wave moving over an uneven bottom. *Proc. Camb. Philos. Soc.,* **73,** 183–203, doi:10.1017/S0305004100047605.

Leith, C. E., 1996: Stochastic models of chaotic systems. *Physica D,* **98,** 481–491, doi:10.1016/0167-2789(96)00107-8.

Li, Q., and D. M. Farmer, 2011: The generation and evolution of nonlinear internal waves in the deep basin of the South China Sea. *J. Phys. Oceanogr.,* **41,** 1345–1363, doi:10.1175/2011JPO4587.1.

Marshall, J., A. Adcroft, C. Hill, L. Perelman, and C. Heisey, 1997: A finite-volume, incompressible Navier Stokes model for studies of the ocean on parallel computers. *J. Geophys. Res.,* **102,** 5753–5766, doi:10.1029/96JC02775.

Obregon, M. A., and Y. A. Stepanyants, 1998: Oblique magnetoacoustic solitons in rotating plasma. *Phys. Lett.,* **249A,** 315–323, doi:10.1016/S0375-9601(98)00735-X.

Ostrovsky, L., 1978: Nonlinear internal waves in a rotating ocean. *Oceanology,* **18** (2), 119–125.

Pacanowski, R. C., and S. G. H. Philander, 1981: Parameterization of vertical mixing in numerical models of tropical oceans. *J. Phys. Oceanogr.,* **11,** 1443–1451, doi:10.1175/1520-0485(1981)011<1443:POVMIN>2.0.CO;2.

Pelinovsky, D., and R. H. J. Grimshaw, 1997: Structural transformation of eigenvalues for a perturbed algebraic soliton potential. *Phys. Lett.,* **229A,** 165–172, doi:10.1016/S0375-9601(97)00191-6.

Vlasenko, V. I., and K. Hutter, 2001: Generation of second mode solitary waves by the interaction first mode soliton with sill. *Nonlinear Processes Geophys.,* **8,** 223–240, doi:10.5194/npg-8-223-2001.

——, and W. Alpers, 2005: Generation of secondary internal waves by the interaction of an internal solitary waves with an underwater bank. *J. Geophys. Res.,* **110,** C02019, doi:10.1029/2004JC002467.

——, N. Stashchuk, and K. Hutter, 2005: *Baroclinic Tides: Theoretical Modelling and Observational Evidence.* Cambridge University Press, 351 pp.

Zhao, Z., and M. H. Alford, 2006: Source and propagation of internal solitary waves in the northeastern South China Sea. *J. Geophys. Res.,* **111,** C11012, doi:10.1029/2006JC003644.

——, V. Klemas, Q. Zheng, and X. Yan, 2004: Remote sensing evidence for baroclinic tide origin of internal solitary waves in the northeastern South China Sea. *Geophys. Res. Lett.,* **31,** L06302, doi:10.1029/2003GL019077.